

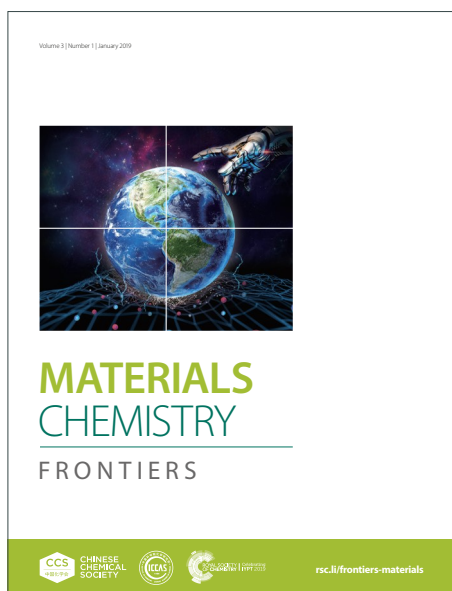
MATERIALS CHEMISTRY

FRONTIERS

Accepted Manuscript



This article can be cited before page numbers have been issued, to do this please use: O. Ola, K. Thummavichai, Y. Chen, N. Wang, Q. niu, J. Wang, S. Sun and Y. Zhu, *Mater. Chem. Front.*, 2022, DOI: 10.1039/D1QM00678A.



This is an Accepted Manuscript, which has been through the Royal Society of Chemistry peer review process and has been accepted for publication.

Accepted Manuscripts are published online shortly after acceptance, before technical editing, formatting and proof reading. Using this free service, authors can make their results available to the community, in citable form, before we publish the edited article. We will replace this Accepted Manuscript with the edited and formatted Advance Article as soon as it is available.

You can find more information about Accepted Manuscripts in the [Information for Authors](#).

Please note that technical editing may introduce minor changes to the text and/or graphics, which may alter content. The journal's standard [Terms & Conditions](#) and the [Ethical guidelines](#) still apply. In no event shall the Royal Society of Chemistry be held responsible for any errors or omissions in this Accepted Manuscript or any consequences arising from the use of any information it contains.

1 Layered Tungsten-Based Composites and Their Pseudocapacitive and Electrocatalytic Performance

2 Oluwafunmilola Ola^{a*}, Kunyapat Thummavichai^b, Yu Chen^{b,c}, Nannan Wang^b, Qijian Niu^d, Jiaao Wang^e,
3 Shibin Sun^f and Yanqiu Zhu^b4 ^aFaculty of Engineering, The University of Nottingham, University Park, Nottingham, NG7 2RD, United
5 Kingdom6 ^bGuangxi Institute Fullerene Technology (GIFT), Key Laboratory of New Processing Technology for
7 Nonferrous Metals and Materials, Ministry of Education, School of Resources, Environment and
8 Materials, Guangxi University, Nanning, 530004, China9 ^cCollege of Engineering, Mathematics and Physical Sciences, University of Exeter, EX4 4QF, UK10 ^dSchool of Agricultural Equipment Engineering, Jiangsu University, Zhenjiang, Jiangsu, 212013, China11 ^eSchool of Material Science and Engineering, University of Jinan, Jinan, 250022, China12 ^fCollege of Logistics Engineering, Shanghai Maritime University, Shanghai 201306, China13 *Corresponding author. Tel: +44 1157 487264. E-mail: Oluwafunmilola.Ola1@nottingham.ac.uk

14 Abstract

15 With the rapid development of heterostructured electrocatalysts, the potential application of
16 transition metal dichalcogenide (TMD)-based composites for electrocatalysis have attracted intense
17 attraction owing to their unique optical, electronic, and mechanical properties. Herein, a facile
18 solvothermal method to obtain heterostructured composites consisting of TMD (WS₂) and graphitic
19 carbon nitride (g-C₃N₄) is reported. DFT calculation results demonstrates that the interface interaction
20 between g-C₃N₄ and WS₂ optimizes the electronic structure of composite materials and activates the
21 active sites. The WS₂ - g-C₃N₄ composites with surface sulfur and nitrogen vacancies exhibit high
22 specific capacitance of 1156 F g⁻¹ and excellent cycling stability with no capacitance loss over 2000
23 charge-discharge cycles, demonstrating huge potentials in applications for pseudocapacitive energy
24 storage. In addition, WS₂ - g-C₃N₄ composites can attain excellent hydrogen production activity to
25 reach a current density of 10 mA cm⁻² at overpotential of -0.170 V (vs. RHE) and Tafel slope of 59 mV
26 dec⁻¹. This work provides an effective way for the synthesis of heterostructured electrocatalysts with
27 efficient activity for energy conversion and storage.

28 Keywords: Tungsten; Heterostructures; Supercapacitors; Hydrogen Evolution Reaction; Graphitic
29 carbon nitride30 **1. Introduction**31 Two-dimensional (2D) layered transition metal dichalcogenides (TMDs) have emerged as a promising
32 class of catalysts due to their unique crystal structure and layer-dependent optoelectronic properties

33 which offer great prospects for exploitation in applications ranging from photovoltaics, photocatalysis
34 to electrocatalysis. Among TMDs, tungsten and its compounds (i.e., WS_x) have been tested as
35 electrocatalysts in their intrinsic or hybrid form, because of their polymorphic nature and ability to
36 participate in complex interatomic interactions with other materials via surface engineering. The
37 structural features of WS_x , such as their lateral size, layer number and active sites i.e. step edges and
38 atomic vacancies, have been shown to greatly influence their electrocatalytic properties and
39 performance [1]. When the lateral size of WS_x is reduced within the nanoscale domain, unique
40 mechanical and optoelectronic properties arising from quantum confinement effects have been
41 observed [2]. Their individual sandwich layers made up of transition metal and chalcogen bound by
42 weak van der Waals forces can also offer large surface area and permeable channels for ion adsorption
43 and transport [3].

44 Experimental and computational studies have established that exposed chalcogen edge sites of WS_x
45 can facilitate improved electrocatalytic performance while the basal surfaces remain catalytically inert
46 [3, 4]. Accordingly, WS_x can be supported on carbon nanostructures to increase the activity of the inert
47 basal surface of TMD through increased defect sites created via the preferential bonding between the
48 basal planes of WS_x and carbon surfaces. Carbon nanostructures can also serve as conductive supports
49 to further augment the electrical conductivity while increasing contact resistance. Pure carbon and
50 hybrids of graphitic carbon nitride ($g-C_3N_4$) have been reported to hold great promise as alternatives
51 to expensive precious metal-based catalysts for water splitting and CO_2 reduction due to their tunable
52 chemistry, high thermal and chemical stability, low cost, and non-toxicity [5, 6].

53 Several strategies have been developed to tailor the structural features of $g-C_3N_4$ to enhance their
54 electrochemical activity and durability. Improvements in electronic structure and energy band
55 configuration of $g-C_3N_4$ based nanocomposites have been demonstrated by the functionalization of $g-$
56 C_3N_4 at atomic and molecular levels via elemental doping and copolymerization, respectively. The
57 content of heteroatomic species of nitrogen and sulfur are particularly useful for modifying surface
58 functional groups and crystallinity which can increase charge carrier mobility with low diffusion
59 barriers during cycling to enhance rate capability and electrochemical performance. For example,
60 quaternary nitrogen has been reported to improve electrical conductivity which facilitates
61 charge/discharge process while pyrrolic and pyridinic nitrogen can introduce active sites and defects
62 [7, 8]. Surface sulfur vacancies have been reported to alter the electronic structure of host materials
63 by reducing the electron transition energy barrier and enhancing electrophilic adsorption [9]. Other
64 ways of improving the physicochemical properties of $g-C_3N_4$ for target-specific applications include
65 coupling with other semiconductors, metal/metal oxides as a cocatalyst or incorporation of
66 carbonaceous materials to form hybrid nanocomposites. Since $g-C_3N_4$ possesses an analogous layered

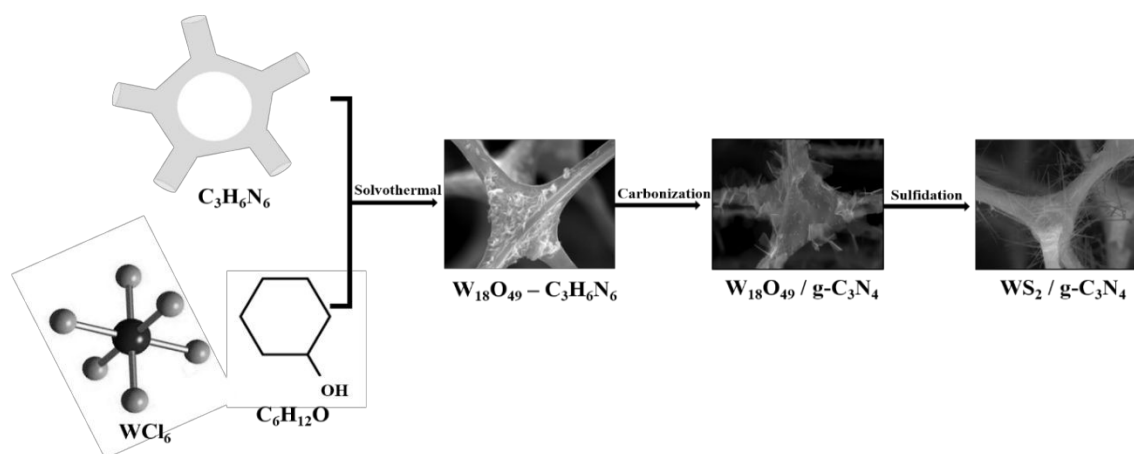
67 structure with finite exposed edges, the fabrication of an organic/inorganic hybrid nanocomposites
68 with another layered material such as WS_2 can lead to the formation of surface heterojunctions for
69 efficient charge collection and separation while exposing active sites required for electrocatalytic
70 reactions. The understanding the effect of growing WS_2 on g- C_3N_4 based support for electrocatalytic
71 reactions is crucial, and yet remains to be explored.

72 Herein, we report the formulation of tungsten-based composites via the growth of WS_2 on
73 interconnected, macroscopic g- C_3N_4 scaffold using $W_{18}O_{49}$ derived from solvothermal treatment as a
74 template. The presence of different heteroatomic surface species of nitrogen and sulfur were found
75 to influence the rate capability and cyclic performance of the tungsten-based composites. DFT
76 calculations confirm the importance of WS_2 - g- C_3N_4 heterostructure design. Benefitting from optimal
77 specific surface area and nitrogen and sulfur content of 11 at% and 1.01 at%, respectively, the WS_600
78 composite exhibit high specific capacitance of 1156 F g^{-1} and excellent cycling stability with no
79 capacitance loss over 2000 charge-discharge cycles, demonstrating huge potentials in applications for
80 pseudocapacitive energy storage. In addition, WS_600 composite can attain excellent hydrogen
81 production activity to reach a current density of 10 mA cm^{-2} at overpotential of -0.170 V and Tafel
82 slope of 59 mV dec^{-1} .

83 2. Experimental

84 2.1. Preparation of WS_2 -g- C_3N_4 composites

85 The scheme for fabricating the WS_2 - g- C_3N_4 composites is illustrated in Figure 1. All chemical
86 compounds and solvents used during synthesis were purchased from Sigma Aldrich. Solvothermal
87 treatment, an easy and low-cost methodology, was employed to grow $W_{18}O_{49}$ on melamine ($C_3H_6N_6$)
88 scaffold using the tungsten hexachloride (WCl_6 , 0.075g) - cyclohexanol ($C_6H_{12}O$, 50ml) mixture,
89 subjected to heat treatment for 6 h at $200 \text{ }^\circ\text{C}$ [10].



91 Figure 1. Schematic of synthetic procedure for WS₂-g-C₃N₄ composites

View Article Online
DOI: 10.1039/D1QM00678A

92 Prior to sulfidation, the W₁₈O₄₉ - C₃H₆N₆ composites were subjected to carbonization under argon
93 atmosphere to yield W₁₈O₄₉ - g-C₃N₄ composites at reaction temperatures of 400, 600 and 800°C to
94 derive samples, which were referred to as WS_400, WS_600 and WS_800, respectively. Once the
95 reaction temperature mentioned above was attained, hydrogen sulfide gas was introduced into the
96 reaction chamber for 50 mins to initiate the sulfidation process for the samples. After sulfidation, most
97 of the W₁₈O₄₉ grown on the g-C₃N₄ scaffolds were converted into WS₂, depending on the reaction
98 temperature.

99 2.2. Materials Characterization and Electrochemical Testing

100 The crystalline structure of the composites was characterized by X-ray diffraction (XRD) using a Bruker
101 D8 Advance diffractometer (operated at 40 kV, 40 mA), with a Cu K α radiation, at a step size of 0.02°
102 and a dwell time of 1 s. The Raman spectra were acquired at room temperature using a Renishaw
103 benchtop system, with 532 nm excitation wavelength and 2400 l mm⁻¹ grating. Surface chemical
104 analysis was performed on a Kratos Axis Ultra system with a monochromated Al Kr X-ray source
105 operated at 10 mA emission current and 15 kV anode potential. Scanning electron microscopy (SEM),
106 transmission electron microscopy (TEM), Raman spectroscopy, X-ray diffraction (XRD) and X-ray
107 photoelectron spectroscopy (XPS) were used to conduct the morphological and structural analyses.
108 Elemental composition of WS₂ - g-C₃N₄ composites was evaluated using scanning electron microscopy
109 (Hitachi S3200N, Oxford instrument - SEM-EDS) and high-resolution transmission electron microscopy
110 (JEOL-2100, HR-TEM), respectively. The Brunauer–Emmett–Teller (BET) surface areas and pore size
111 distribution of the WS₂/g-C₃N₄ composites were measured with the Micromeritics ASAP 2020 nitrogen
112 adsorption analyzer.

113 2.3. Electrochemical Measurements

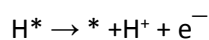
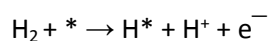
114 Electrochemical measurements for hydrogen evolution reaction (HER) and capacitance were
115 performed at room temperature using a CHI-660E workstation coupled with a rotating disk electrode
116 (RDE) system consisting of Ag/AgCl/KCl, platinum wire and glassy carbon rotating disk electrode (GCE)
117 covered with catalyst ink as reference, counter and working electrodes, respectively. The working
118 electrode was prepared by drop casting of catalyst ink prepared from a mixture of 5 μ L of Nafion
119 solution, 1mL of ethanol/water solution and 3 mg of composite sample. The active mass loading of
120 the electrodes was 0.21 mg cm⁻². For the HER, electrochemical measurements were carried out in a
121 0.5 M H₂SO₄ (Sigma Aldrich) electrolyte solution at different potentials and scan rates varying from 0
122 – -0.8 V and 10 – 100 mV, respectively. The experimentally measured potential versus Ag/AgCl, $E_{\text{Ag/AgCl}}$,
123 was calibrated with respect to the RHE (reversible hydrogen electrode), E_{RHE} , according to the Nernst
124 equation; $E_{\text{RHE}} = E_{\text{Ag/AgCl}} + E_{\text{Ag/AgCl}}^0 + 0.059 \text{ pH}$ (at 25 °C) where $E_{\text{Ag/AgCl}}^0 = 0.1976 \text{ V}$ at 25 °C. The acquired

125 HER experimental values were generated in 0.5 M H₂SO₄ solution and corrected for IR View Article Online
DOI: 10.1039/D1QM00678A
126 loss. Chronoamperometric measurements were performed by applying the corresponding potential
127 to support an initial current density of about 10 mA cm⁻² for 10 h for the HER. Electrochemical
128 impedance spectroscopy measurements were carried out after applying the AC voltage with 10 mV
129 amplitude at a frequency range of 0.05 Hz to 10 kHz, using the open circuit potential.

130 For specific capacitance (C_{sp}), galvanostatic discharge/charge (GCD) measurements were recorded at
131 current densities ranging from 2 to 15 A g⁻¹. Specific capacitance (C_{sp}) was derived from GCD
132 measurements using the equation: C_{sp} = I/m (ΔV/Δt) where I (A) is the discharge current, Δt (s) is the
133 discharge time consumed in the potential window of ΔV (V) and m represents the mass of active
134 material. The stability of the supercapacitor was evaluated by cyclic GCD measurements at current
135 density of 15 A g⁻¹ for 10 000 cycles.

136 2.4. DFT Calculation Parameters

137 In this work, the first-principles density functional theory (DFT) was applied by using the projector
138 augmented wave method (PAW) [11]. Additionally, the exchange-correlation function was approved
139 by employing the Perdew-Burke-Ernzerhof generalized gradient approximation (PBE-GGA) [12]. For
140 the results, we applied the wave functions with plane-wave expansion with 400 eV cutting off energy
141 while force tolerance was set at 0.05eV/Å for relaxation. Also, certain surfaces of the (100) planes
142 were chosen to build the heterostructure of WS₂ - g-C₃N₄ nanocomposites. Furthermore, the WS₂
143 surface of (100) with 7 × 7 units of and the g-C₃N₄ surface (100) with 3 × 3 units were established to
144 simulate the heterostructure of WS₂ - g-C₃N₄. Since HER consists of four elementary reactions, the
145 electron transfer for each reaction was supplemented by the process of proton expulsion, which can
146 be indicated below:



149 where * and X* are demonstrated as an adsorption site and an adsorbed X intermediary on the
150 reaction surface. The H⁺ + e⁻ can be shown as free energy of half formation energy of H₂ at 1 atm
151 within 298 K. The reduction activity was calculated by using ΔG = ΔE + ΔZPE - TΔS for the free energy
152 where the ΔE was acquired by its geometric forms. Moreover, the ΔZPE and ΔS were defined by using
153 the computational vibration frequency, combined with the standard tables of gas reactants. The
154 entropy was assumed as zero at the adsorbed surface-active site.

155 3. Results and Discussion

156 3.1 Structural and Physicochemical Properties

157 To investigate the structure-activity relationships, DFT calculations were applied to study the
 158 electronic structure of these catalysts. Here, $g\text{-C}_3\text{N}_4$, WS_2 and $\text{WS}_2 - g\text{-C}_3\text{N}_4$ are considered as the model
 159 object to analyse the difference of electronic structure and catalytic mechanism. Density of states
 160 (DOS) and partial density of states (PDOS) of these materials are shown in Figure 2.

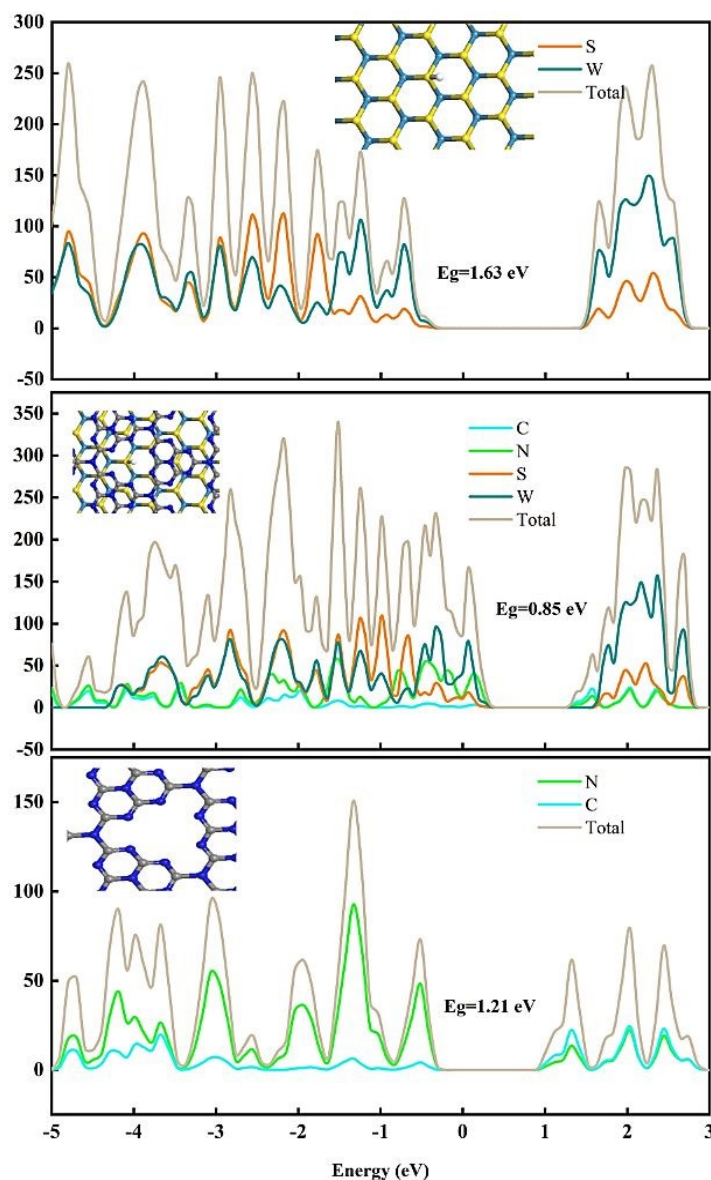
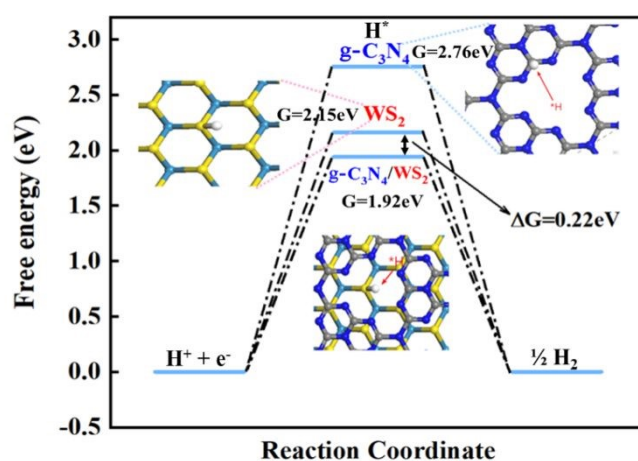


Figure 2. Theoretical calculation of the density of states (DOSs) near the Fermi level

161 The band gap of WS_2 , $g\text{-C}_3\text{N}_4$, and $\text{WS}_2 - g\text{-C}_3\text{N}_4$ are 1.63 eV, 1.21 eV, and 0.85 eV, respectively. The WS_2
 162 - $g\text{-C}_3\text{N}_4$ composite exhibits the lowest band gap energy, beneficial to electron transfer in catalytic
 163 process. Furthermore, atomic orbit such as N, S, and W of the $\text{WS}_2 - g\text{-C}_3\text{N}_4$ composite is closer to the
 164 Fermi level compared with $g\text{-C}_3\text{N}_4$ and WS_2 , which supports this finding. In addition, enhanced electron
 165 transfer at the interface of $g\text{-C}_3\text{N}_4$ and WS_2 can further facilitate the absorption of water molecules.

166 Therefore, designing the heterostructure of WS_2 - $g-C_3N_4$ has a positive effect for improving the
 167 catalytic activity of HER. To understand the catalytic process for HER reaction, the reaction energies
 168 of WS_2 , $g-C_3N_4$, and WS_2 - $g-C_3N_4$ at each step of the HER reaction are calculated. The Gibbs free
 169 energies of pristine $g-C_3N_4$, WS_2 and WS_2 - $g-C_3N_4$ composite have been calculated to investigate HER
 170 activity (Figure 3). As shown in Figure 3, the Volmer-Heyrovsky reaction pathway of HER is that H^+ was
 171 first adsorbed onto the surface of solid catalysts, then formed in the intermediate species H^* , finally
 172 converted into hydrogen.

173

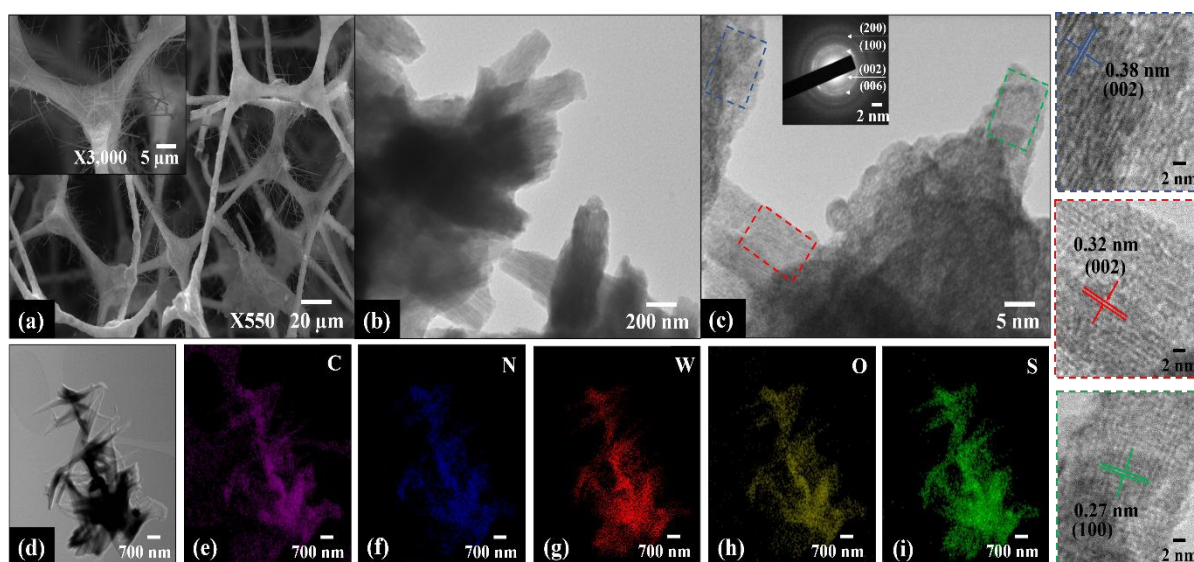


174 Figure 3. Free-energy diagram for the HER with Volmer-Heyrovsky reactions on pristine $g-C_3N_4$, WS_2
 175 and WS_2 - $g-C_3N_4$ composite.

176 In Volmer-Heyrovsky reaction, the generation of intermediate species H^* is the important rate
 177 determining step in the HER reaction and needs to overcome some reaction energy barriers. Figure 3
 178 displays the calculated Gibbs free energy (ΔGH^*) of hydrogen adsorption (0.2 2eV) and the Gibbs free
 179 energy of C_3N_4 , WS_2 and C_3N_4/WS_2 , which are 2.76 eV, 2.14 eV and 1.92 eV, respectively, which is in
 180 line with previous reported values [13]. The WS_2 - $g-C_3N_4$ composite shows the lowest activation
 181 barriers than those of WS_2 and $g-C_3N_4$, indicating that the WS_2 - $g-C_3N_4$ possesses the highest
 182 electrocatalytic HER activity. Our calculation results also demonstrate that the interface interaction
 183 between $g-C_3N_4$ and WS_2 optimizes the electronic structure of composite materials via the promotion
 184 of more electrochemical active sites and improved charge transfer kinetics required for optimal
 185 electrochemical performance. These calculation results confirm the importance of WS_2 - $g-C_3N_4$
 186 heterostructure design.

187 As shown in Figure 4a and S1, a sparse to dense mat of nanowires was grown on the $g-C_3N_4$ scaffolds
 188 when the calcination temperature increased from 400-800 °C, respectively. The average thickness and
 189 length of the nanowires were between 10-30 nm and $\leq 1 \mu m$, respectively. Low- and high-resolution

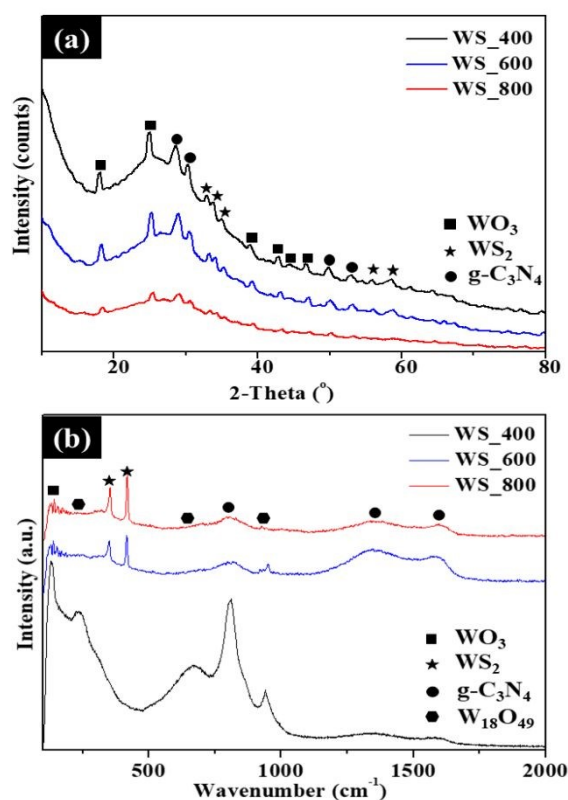
190 TEM images show homogeneous, layered, spindle-shaped structures of varying width and length
 191 stacked on top of each other in different directions (Figure 4b). The interplanar spacing of the spindle
 192 shaped structures are 0.38, 0.32 and 0.27 nm which matched the d spacing values for (002), (002) and
 193 (100) planes of $g\text{-C}_3\text{N}_4$, orthorhombic (β) WO_3 and hexagonal WS_2 , respectively [14]. The presence of
 194 WO_3 is due to the reaction of some $\text{W}_{18}\text{O}_{49}$ nanoparticles with residue oxygen during the reduction
 195 reaction in $\text{H}_2\text{S}/\text{Ar}$ atmosphere between 400-800 °C. The phase transformation of $\text{W}_{18}\text{O}_{49}$ is expected
 196 to initially proceed through the formation of WS_3 via the substitution of oxygen atoms with sulphur
 197 atoms [15]. Further reaction leads to the formation of WS_2 with residual orthorhombic WO_3
 198 nanoparticles due to oxidation occurring during sulfidation. The presence and homogeneous
 199 distribution of C, N, W, O and S was clearly confirmed from the elemental mapping of WS_2 _800 (Figure
 200 4d – i) which is consistent with the XRD and XPS results, to be described below.



201 Figure 4. (a) SEM image of WS_2 - $g\text{-C}_3\text{N}_4$ composites prepared at 800 °C (WS_800), with inset high-
 202 resolution image showing the nanowire morphology of WS_800 . TEM analysis of WS_800 : (b) low
 203 magnification image, (c) high-resolution images showing lattice planes of $g\text{-C}_3\text{N}_4$, WO_3 and WS_2 . (d-i)
 204 TEM images with corresponding elemental mapping of WS_800 .

206 The XRD patterns of the as-synthesized WS_2 - $g\text{-C}_3\text{N}_4$ composites prepared after thermal treatment at
 207 400-800°C are shown in Figure 5a. Phase characterization indicates that the samples are crystalline
 208 and in good agreement with orthorhombic (β) WO_3 (JCPDS card no. 20-1324), $g\text{-C}_3\text{N}_4$ (JCPDS no. 87-
 209 1526), and hexagonal WS_2 (JCPDS card no. 08-0237). The diffraction peaks at $2\theta = 32.8^\circ$, 33.6° , 35.3° ,
 210 55.9° and 57.6° are indexed to (100), (101), (102), (106) and (110) planes of hexagonal WS_2 ,
 211 respectively. The diffraction peak at 27.6° is attributed to the (002) plane of $g\text{-C}_3\text{N}_4$ linked to the
 212 interplanar stacking of conjugated aromatic systems [16]. The peaks of $\beta\text{-WO}_3$ and WS_2 become

213 sharper with the increase of reaction temperatures. Raman spectra in Figure 5b have revealed the
 214 characteristic peaks of the $W_{18}O_{49}$ and WS_2 in the 200-1000 cm^{-1} range and the D (1348 cm^{-1}) and G
 215 (1587 cm^{-1}) bands for $g-C_3N_4$ in the WS_2 - $g-C_3N_4$ composites prepared at different temperatures. The
 216 peak intensity ratios of the disordered amorphous carbon (D band) to graphitic carbon (G band) are
 217 calculated to be 1.33, 1.23 and 1.07 for WS_{400} , WS_{600} and WS_{800} , respectively. The absence of
 218 2D band linked to second-order two-phonon process of graphene and low degree of
 219 graphitization is ascribed to the presence of structural defects and high nitrogen content.



220
 221 Figure 5. (a) XRD patterns and (b) Raman spectra of the WS_2 - $g-C_3N_4$ composites prepared at different
 222 temperatures.

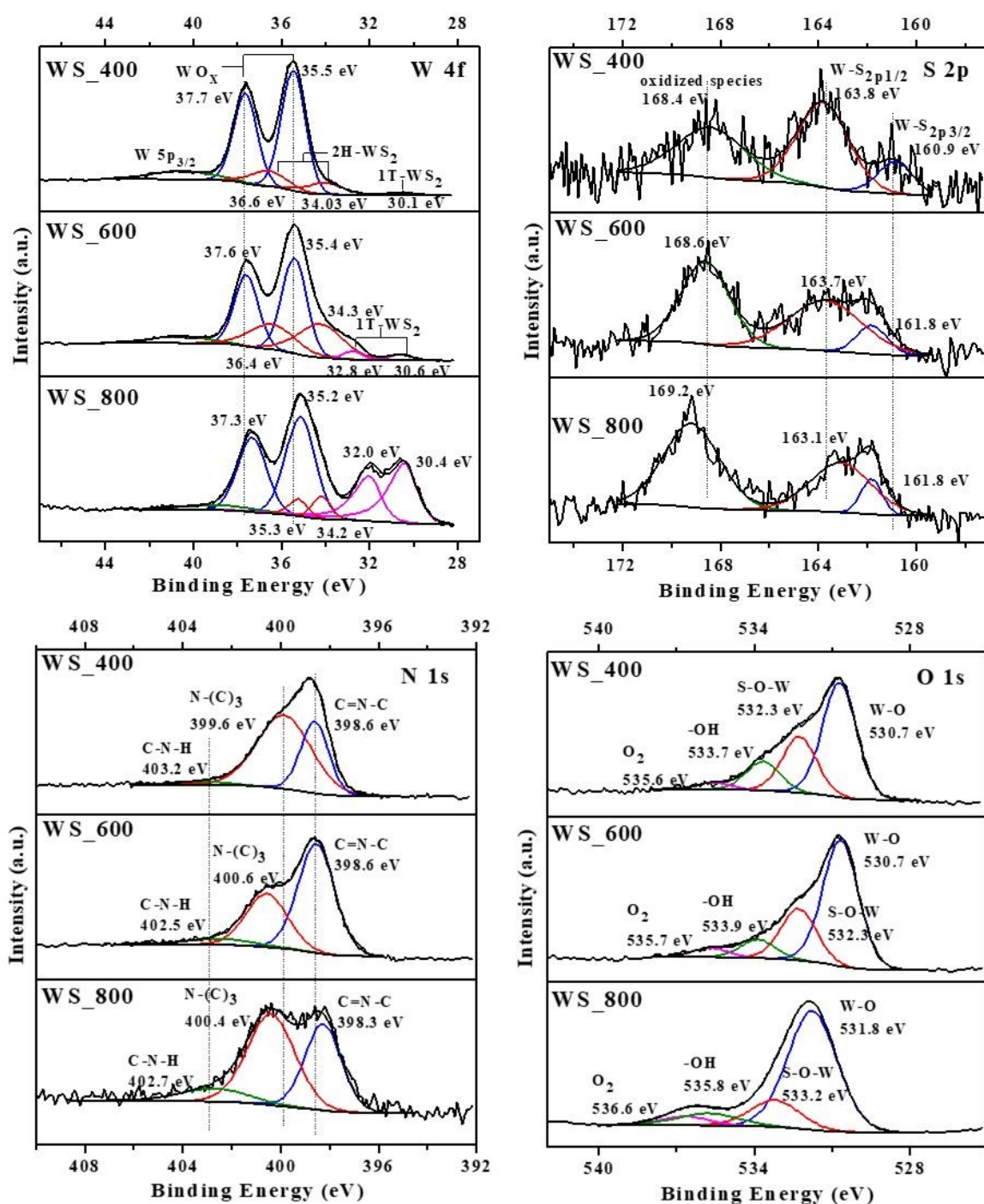
223 Only WS_{400} presents a Raman band at 129 cm^{-1} , which is assigned to the β - WO_3 phase. This confirms
 224 that some oxidation reaction occurred during the growth of WS_2 on the $g-C_3N_4$ scaffold. The 226 cm^{-1}
 225 band could be assigned to the O-W-O bending mode of bridging oxygen for $W_{18}O_{49}$. The characteristic
 226 Raman bands for $W_{18}O_{49}$ observed at 667 and 812 cm^{-1} are assigned to the asymmetric and symmetric
 227 stretching vibration modes of O-W-O, respectively. The Raman bands at 812 cm^{-1} can be attributed to
 228 the out-of-plane N-C-N bending of $g-C_3N_4$. This band at 920-1000 cm^{-1} corresponds to the W=O
 229 stretching vibration mode of a terminal oxygen and has been used as the characteristic shifts for
 230 $W_{18}O_{49}$ nanowires [17]. The intensity of this band was observed to decrease with increasing
 231 temperatures, due to the conversion of most of the $W_{18}O_{49}$ into WS_2 . The disappearance of the 129,

232 225 and 667 cm^{-1} characteristic bands of $\beta\text{-WO}_3$ and $\text{W}_{18}\text{O}_{49}$, respectively, was observed for the
233 WS_600 and WS_800 samples. As shown in Figure 5b, additional bands were observed for WS_600
234 and WS_800 at 297, 350 and 416 cm^{-1} which corresponds to the E_{1g} , E_{2g}^1 and A_{1g} modes of WS_2 ,
235 respectively. The E_{2g}^1 mode is linked to the in-plane, while A_{1g} mode correspond to out-of-plane
236 phonon mode of WS_2 . Additionally, the A_{1g} mode undergoes a slight red shift as the reaction
237 temperature was increased from 600 to 800°C. This shift triggered by the temperature increase is
238 expected, due to the decrease in the interlayer Van der Waals interaction resulting in weak restoring
239 forces during lattice vibration. The BET surface area of the $\text{WS}_2\text{-g-C}_3\text{N}_4$ composites and pore size
240 distribution of WS_600 is shown in Fig. S2. The resulting specific surface areas of WS_400, WS_600
241 and WS_800 was 61, 86 and 47 $\text{m}^2 \text{g}^{-1}$, respectively. As shown in Fig. S2b, WS_600 possesses
242 mesopores with pore sizes of less than 37 nm which can facilitate efficient ion transport and
243 accommodate the potential volume changes during the repeated charge–discharge processes.

244 The chemical composition and valence state of the composites are characterized by XPS. The atomic
245 percentage of all samples, with the calculated atomic ratios for N/C, pyridinic N [C-N-C]/pyrrolic N [N-
246 (C)₃], W/S and WO_3/WS_2 are summarized in Table S1. The survey scan spectrum in Figure S2a confirms
247 that C, N, O, W and S elements exist in WS_600. Considering the W 4f spectra of all samples, the
248 binding energy at about 35 and 37 eV were generally attributed to W^{6+} species of tungsten oxide
249 (WO_x). Two peaks of W $4f_{7/2}$ and W $4f_{5/2}$ at about 34 and 36 eV can be observed, indicating the
250 semiconducting nature of the 2H phase WS_2 . The peak locations are positively shifted to higher binding
251 energies compared with the reference for 2H- WS_2 which is matched with the peak of W^{5+} in the WO_x
252 structure [18]. However, the peak of one layer per (Trigonal) unit cell (1T) structure is observed in all
253 samples. Together with the XRD results and TEM element mapping, these peaks are therefore
254 assigned to 2 layers per hexagonal unit cell (2H)-phase of WS_2 . The peak shift is linked to an incomplete
255 transfer structure from WO_x to WS_2 , and to the presence of W^{5+} species inside the WO_x structure.

256 The peaks at 30 and 32 eV can be attributed to metallic 1T- WS_2 structures or sulphur vacancies in the
257 crystal structure [19], which are present in both WS_600 and WS_800 samples. However, a shadow
258 peak of the 1T phase WS_2 is also presented at 30.1 eV for WS_400 samples. The peak of W $5p_{3/2}$ at
259 40.5 eV is attributed to the unavoidable surface oxidation of the samples. The S 2p spectra were
260 deconvoluted into 3 peaks for all samples, which include S $2p_{3/2}$ peak at ~161 eV, S $2p_{1/2}$ peak at ~163
261 eV and the oxidized species at ~169 eV. The oxidised sulphate groups were generated from residues
262 after reaction or intermediate products formed during the transformation of WS_2 from WO_x [20]. The
263 peak percentage areas for both S $2p_{3/2}$ and S $2p_{1/2}$ in the sample decreased with increased temperature
264 from 400 to 800 °C, i.e., WS_400 to WS_800. As shown in Table S1, S content of the composites

265 decreases with increasing calcination temperature. The same decreasing trend was observed for the
 266 atomic ratios of W to S, implying the absence of surface sulphur atoms.



267
 268 Figure 6. High-resolution XPS spectra of (a) W4f, (b) S 2p, (c) N 1s and (d) O 1s for all samples.

269 The O 1s spectra of mixed WO_x/WS_2 nanostructures can be assigned into 4 peaks with binding energies
 270 of about 530, 532, 533 and 535 eV [6]. The peak at 530 eV is attributed to binding state of W^{6+} or W^{5+}
 271 corresponding to the lattice oxygen in WO_x ; while the peak at 533 eV is from O_2 adsorbed on the

272 WO_x/WS_2 . The peak at 535 eV is assigned to OH-groups and water molecules, which can be
273 chemisorbed on the defects and vacancies of the WO_x/WS_2 nanostructures. The peak at 322 eV can
274 be associated with the O atom bonded to W atoms, which corresponded to S-O-W bonds indicating
275 that an interfacial bond exists in the nanostructures [21].

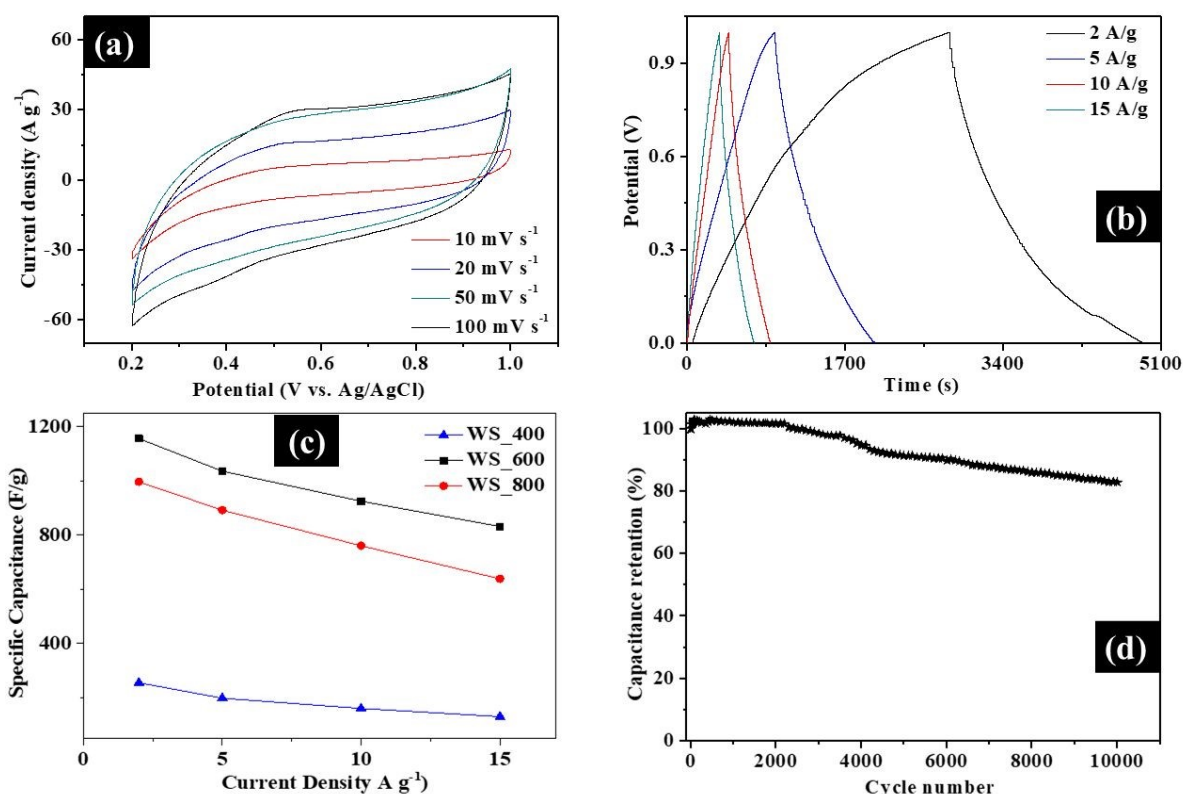
276 According to the high resolution XPS spectra of N 1s, three peaks at about 398, 399 and 402 eV
277 corresponding to the sp^2 -bonded pyridinic N (C=N-C), pyrrolic N (N-(C)₃) groups and quaternary N (C-
278 N-H), respectively [22]. The composites possess high N contents between 5.31 and 17at%, showing
279 that high N amounts are present in the final structures after calcination at 800°C. As shown in Table
280 S1, the N/C atomic ratio was observed to decrease from 0.24 to 0.065 with increasing calcination
281 temperature. The same decreasing trend was observed for atomic ratios of pyridinic and pyrrolic N
282 species where the atomic ratios decreased from 1.99 to 0.73 for WS_400 to WS_800, respectively.
283 Conversely, an increasing trend was observed for the quaternary N (Figure S4). The decreasing N
284 content can be linked to the introduction of N-vacancies while preferential loss of pyridinic N atoms
285 over pyrrolic N atoms occurs due to unsaturated coordination which creates charge imbalance due to
286 missing pyridinic N atoms [23]. The type and content of pyridinic, pyrrolic and quaternary N species
287 have been reported to play a key role in influencing the structure (i.e., defects and active sites) and
288 electrochemical performance (i.e., electron transport and conductivity) [7, 23]. As shown in Figure S4,
289 the WS_2 - $g-C_3N_4$ composites possess a high content of pyridinic and pyrrolic N species, which can
290 provide active sites for redox reactions, resulting in improved electrochemical performance.

291 As shown in Figure S3b, the core level spectrum of C 1s can be fitted with 4 peaks with positions
292 around 284, 285, 287 and 290 eV, which are corresponding to the C-C, C-O/C-S, N=C-N and C-N bonds,
293 respectively [24]. Therefore, all the structure analyses suggest that the WS_2 - $g-C_3N_4$ composites contain
294 mainly 2D WS_2 with residual amounts of WO_x . The amount of WS_2 (2H-phase) in the samples increased
295 with the increases of temperature from 400 to 600 °C while the amount of WS_2 (2H-phase) in the 800
296 °C sample decreased, due to phase transformation of 2H to 1T. Overall, the total WO_3/WS_2 atomic
297 ratio of the composites decreased with increased calcination temperature (Table S1). The peaks of N
298 and C confirmed the presence of graphitic carbon nitride within these samples.

299 Based on the XPS results, it is confirmed that WO_x/WS_2 was grown on the $g-C_3N_4$ surface and
300 connected via Van der Waals bonds. In addition, the 2H- WS_2 matrix contained S-vacancies due to WO_x -
301 WS_5 or 2H-1T phase transitions. This is supported by O 1s peak at about 322 eV), 1T (which can also
302 refer to defects of WS_5 structure) and oxidized species peaks from S 2p spectra [25]. Overall, the
303 preferential bonding between the basal planes of WS_2 and $g-C_3N_4$ optimizes the electronic structure
304 of the composite materials and activates the active sites.

305 **3.2 Electrochemical Performance Evaluation**

306 The electrochemical performance of the WS₂ - g-C₃N₄ composites for supercapacitors was evaluated
 307 by using a three-electrode cell configuration in 0.5M H₂SO₄ electrolyte. Figures 7 and S5 show the
 308 electrochemical performance of the WS₂-g-C₃N₄ composites. As shown in Figure 7a, S4a and c, all WS₂-
 309 g-C₃N₄ composites possess a convex quasi-rectangular CV shape at potential windows of 0.2 to 1.0V
 310 at various scan rates ranging from 10 to 100 mV s⁻¹, which is indicative of the pseudocapacitive
 311 behavior, due to the electric double layer capacitance (EDLC) and Faradaic reactions of g-C₃N₄ and
 312 WS₂, respectively.



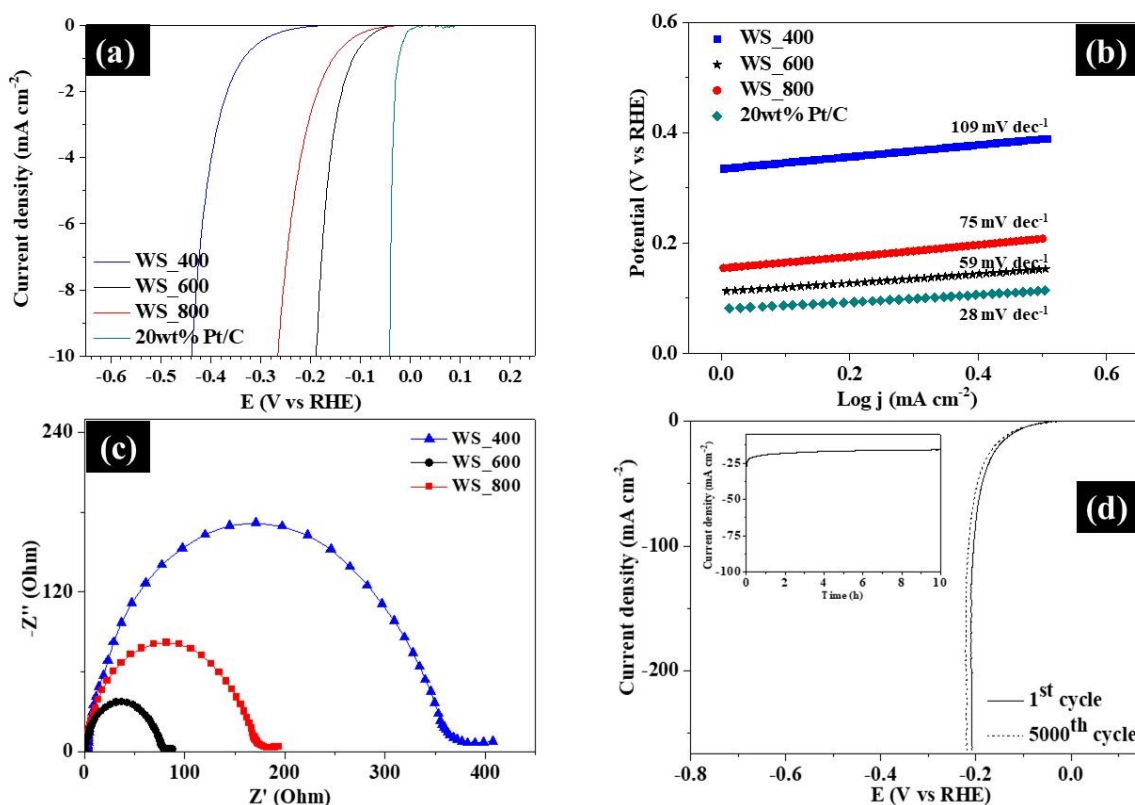
313
 314 Figure 7. (a) CV curves of the WS₆₀₀ electrode at various scan rates from 10 to 100 mV s⁻¹, (b)
 315 Galvanostatic charge discharge curves of WS₆₀₀ electrodes at different current densities, (c) Specific
 316 capacitance of WS₂-g-C₃N₄ composites as a function of current densities, and (d) Cyclic performance
 317 of WS₆₀₀ electrode at 15 A g⁻¹.

318 The shape of the well-defined CV curves is maintained at different scan rates, which indicates the
 319 capacity of the WS₂ - g-C₃N₄ composites for fast charge transfer and improved rate performance. The
 320 galvanostatic charge/discharge profiles of WS₄₀₀, WS₆₀₀ and WS₈₀₀ electrodes at current
 321 densities between 2-15 A g⁻¹ were measured and presented in Figures 7b, S5b and d, to evaluate the
 322 potential use of these composites as supercapacitors. The quasi-triangle shape of galvanostatic

323 charge/discharge profiles is asymmetrical, suggesting the presence of some EDLC and Faradaic
324 reactions, which is consistent with the reported CV results. The WS₂/600 electrode exhibited a longer
325 discharge time compared with other electrodes, supporting an optimal pseudocapacitive
326 performance. The specific capacitance was calculated from the galvanostatic charge/discharge
327 profiles of the WS₂-g-C₃N₄ electrodes, to highlight the rate capability which represents a measure of
328 the charge and discharge capability of supercapacitors. The calculated specific capacitance values of
329 WS₂-g-C₃N₄ electrodes at different current densities are shown in Figure 7c. The electrodes of samples
330 WS₂/400, WS₂/600 and WS₂/800 reveal specific capacitance values of 256, 1156 and 997 F g⁻¹ when the
331 N content was 17, 11.78 and 5.31 at%, respectively at a current density of 2 A g⁻¹. The specific
332 capacitance values show that the nitrogen content must be kept around 11.78 at% to obtain optimal
333 specific capacitance values. WS₂/600 electrode with N and S content of 11 at% and 1.01 at% had the
334 maximum specific capacitance compared with other electrodes. Its specific capacitance remained as
335 high as 832 F g⁻¹ at a maximum current density of 15 A g⁻¹, due to its excellent rate capability and
336 electrochemical performance. In comparison, the specific capacitance values of WS₂/400 and WS₂/800
337 electrodes are 639 and 131 F g⁻¹ at the same current density of 15 A g⁻¹. The specific capacitance
338 retention of the WS₂/600 electrode was estimated to be 12.5% and 41% higher than those of WS₂/400
339 and WS₂/800, respectively, revealing the superior rate capability of WS₂/600 electrode. The specific
340 capacitance of all the samples decreases with increasing current density due to the difficulty in ion
341 transport at high current densities. In addition, the electrochemical stability was evaluated via cyclic
342 galvanostatic measurements at a current density at 15 A g⁻¹. The stability of the WS₂/600 electrode
343 over 10,000 cycles at 15 A g⁻¹ is shown in Figure 7d. The WS₂/600 electrode exhibited excellent cyclic
344 stability. After 10,000 cycles, the WS₂/600 electrode retained 82% of its initial specific capacitance. The
345 specific capacitance of WS₂/600 is superior to the recently reported tungsten-based supercapacitors
346 [26-32] (Table S2). Overall, the WS₂/600 electrode possessed the optimal specific capacitance,
347 improved rate capability and cyclic performance, against the WS₂/400 and WS₂/800 electrodes. The
348 improved performance of WS₂/600 electrode is linked to the contributing effects of optimal surface
349 area, surface defects (i.e., sulfur vacancies in WS₂ and nitrogen vacancies in g-C₃N₄) as active sites, and
350 both EDLC and redox reactions from the WS₂ and g-C₃N₄, which together facilitated the improved
351 charge storage. The layered structures of WS₂ embedded in the g-C₃N₄ scaffold provided shorter
352 pathways for a fast and efficient ion transport, while the porous feature could accommodate the
353 potential volume changes during the repeated charge–discharge processes.

354 Besides utilization as supercapacitors, the WS₂-g-C₃N₄ composites also demonstrated interesting
355 performance in hydrogen evolution reaction, which is a key process in the electrochemical water
356 splitting. The electrocatalytic HER activities of the WS₂-g-C₃N₄ composites were evaluated using a

357 three-electrode configuration in an acidic (0.5 M H₂SO₄) electrolyte, as shown in Figure 8. The linear
 358 sweep voltammetry (LSV) curves of 20wt% Pt/C and WS₂ - g-C₃N₄ composites are displayed in Figure
 359 8a. The WS₂_600 electrode again showed a small onset potential of -0.06 V (vs. RHE) against other WS₂
 360 - g-C₃N₄ based electrodes, and was slightly higher than that of 20wt% Pt/C. After which a sharp
 361 increase in the cathodic current was observed under negative potentials for all samples. The operating
 362 potential at a standard current density of 10 mA cm⁻² was adopted in this study, for comparison
 363 purpose. This value is representative of the current density expected for a solar water splitting device
 364 operating at 12.3% efficiency [33]. WS₂_600 electrode exhibited excellent catalytic activity with a low
 365 overpotential of -0.170 V (vs. RHE) to drive a current density of 10 mA cm⁻².



366
 367 Figure 8. (a) Polarization LSV curves, (b) Tafel plots, (c) EIS Nyquist plots and (d) LSV curves of WS₂_600
 368 before and after cyclic studies (inset shows chronoamperometric measurements of WS₂_600).

369 In comparison, the WS₂_400 and WS₂_800 electrodes possessed higher overpotentials of -0.440 and -
 370 0.260 V (vs. RHE), respectively, to attain the same current density. These results affirmed the
 371 exceptional HER electrocatalytic activity of WS₂_600 amongst all samples.

372 The Tafel slopes of the samples were plotted to estimate the reaction kinetics and the rate-
 373 determining step for the HER process. As shown in Figure 8b, the Tafel slope of WS₂_600 was 59 mV
 374 dec⁻¹, much lower than 75 and 109 mV dec⁻¹ for WS₂_800 and WS₂_400, respectively, indicative of its
 375 faster kinetics. The low Tafel slope of WS₂_600 confirmed the favorable HER kinetics, which is linked to

376 its layered structure providing more pathways for easy ion transportation. Hydrogen production for
377 the samples was facilitated through a Volmer-Heyrovsky mechanism due to their Tafel slope values
378 being within the range of 40 and 120 mV dec^{-1} , where electrochemical desorption and formation
379 of hydrogen molecules occurred, respectively. The transition from the Volmer to Heyrovsky pathway
380 is the rate limiting step for this mechanism. The excellent HER performance of WS_600 with low
381 overpotential and Tafel slope is comparable to other previously reported tungsten-based electrodes
382 in the literature [1, 26, 34-38] (Table S3). The reaction kinetics occurring at the electrode/electrolyte
383 interface was evaluated by EIS. Figure 8c shows the Nyquist plots where the WS₂ - g-C₃N₄ based
384 electrodes showed semicircles at high frequency region, a little intercept at the real part and a line
385 with large slope at low frequencies which is attributed to the charge transfer resistance (R_{ct}), intrinsic
386 resistance (R_e), and the diffusion resistance (W), respectively. The WS₂ - g-C₃N₄ based electrodes
387 exhibit low resistance and fast ion transfer, which enhanced pseudocapacitance. The
388 WS_600 exhibited a lower R_{ct} compared with other samples, due to better HER kinetics and enhanced
389 ion transport at the electrode/electrolyte interface. The EIS plots of WS_600 before and after cycling
390 (Figure S6) has a similar trend, where a slight increase of the R_{ct} and R_e was observed after 5000 cycles
391 confirming the stability of WS_600.

392 The durability of WS_600 was investigated by cyclic linear potential sweeps and chronoamperometry
393 measurements at the current density of 20 mA cm^{-2} . The polarization curve of WS_600 after
394 continuous 5000 cycles at a scan rate of 5 mV s^{-1} exhibited only a small decay benchmarked against
395 the initial cycle (Figure 8d). The current-time curve showed that WS_600 was stabilized after 10 h
396 with no attenuation in its current density. These observations indicated that the WS_600 possessed
397 superior cyclic and long-term stability for the HER. Overall, the excellent electrochemical performance
398 was attributed to WS₂ - g-C₃N₄ composites, which provided more electroactive sites at
399 electrolyte/electrocatalyst interface to facilitate effective ion transport and possessed ample active
400 sites to allow intensive electrochemical reactions.

401 4. Conclusions

402 In summary, WS₂ - g-C₃N₄ composites with surface vacancies were successfully prepared by using a
403 facile solvothermal method followed by sulfidation. Experimental and computational studies revealed
404 the preferential bonding and interfacial interaction between the basal planes of WS₂ and g-C₃N₄, which
405 optimizes the electronic structure, improves charge transfer and electrochemical performance. In
406 comparison with other electrocatalysts, WS_600 electrode showed excellent specific capacitance of
407 1156 F g^{-1} at the current density of 2 A g^{-1} , compared with 256 F g^{-1} for WS_400. The WS_600 electrode
408 retained 82% of its initial specific capacitance after 10,000 cycles. In addition to demonstrating

409 excellent specific capacitance, the WS_600 electrode also exhibited an excellent catalytic activity, with
410 a low overpotential of 0.170 V (vs. RHE) capable of driving a current density of 10 mA cm⁻² and a good
411 stability after 8 h of testing. Overall, the WS_600 electrode possessed optimal specific capacitance,
412 improved rate capability and cyclic performance, benchmarked against other samples due to the
413 contributing effects of optimal specific surface area, surface defects (i.e., sulfur vacancies in WS₂ and
414 nitrogen vacancies in g-C₃N₄) as active sites, and both EDLC and redox reactions from the WS₂ and g-
415 C₃N₄, which together facilitated the improved charge storage.

416 Acknowledgements

417 This work was supported by the Leverhulme Trust Early Career Fellowship, ECF-2018-376.

418 References

- 419 [1] B. Seo *et al.*, "Preferential horizontal growth of tungsten sulfide on carbon and insight into
420 active sulfur sites for the hydrogen evolution reaction," *Nanoscale*, 10.1039/C7NR08161H
421 10(2018)3838-3848. 10.1039/C7NR08161H.
- 422
- 423 [2] H. Jin *et al.*, "Colloidal single-layer quantum dots with lateral confinement effects on 2D
424 exciton," *JACS*, 138(2016)13253-13259. 10.1021/jacs.6b06972.
- 425
- 426 [3] L. Wang *et al.*, "Coral-like-Structured Ni/C₃N₄ Composite Coating: An Active Electrocatalyst
427 for Hydrogen Evolution Reaction in Alkaline Solution," *ACS Sustainable Chemistry &*
428 *Engineering*, 5(2017)7993-8003. 10.1021/acssuschemeng.7b01576.
- 429
- 430 [4] D. Zheng, G. Zhang, Y. Hou and X. Wang, "Layering MoS₂ on soft hollow g-C₃N₄
431 nanostructures for photocatalytic hydrogen evolution," *Appl. Catal. A: Gen.*, 521(2016)2-8.
432 <https://doi.org/10.1016/j.apcata.2015.10.037>.
- 433
- 434 [5] K. S. Lakhi *et al.*, "Mesoporous carbon nitrides: synthesis, functionalization, and
435 applications," *Chem Soc Rev*, 46(2017)72-101.
- 436
- 437 [6] J. Duan *et al.*, "Porous C₃N₄ nanolayers@N-graphene films as catalyst electrodes for highly
438 efficient hydrogen evolution," *ACS Nano*, 9(2015)931-940. 10.1021/nn506701x.
- 439
- 440 [7] Q. Shen *et al.*, "Designing g-C₃N₄/N-rich carbon fiber composites for high-performance
441 potassium-ion hybrid capacitors," *Energy & Environ. Mater.*, 4(2020)638-645.
442 <https://doi.org/10.1002/eem2.12148>.
- 443
- 444 [8] J. Wang *et al.*, "A defective g-C₃N₄/RGO/TiO₂ composite from hydrogen treatment for
445 enhanced visible-light photocatalytic H₂ production," *Nanoscale*, 10.1039/D0NR05141A
446 12(2020)22030-22035. 10.1039/D0NR05141A.

447

- 448 [9] H. J. Li *et al.*, "Sulfur vacancies in $\text{Co}_9\text{S}_{8-x}/\text{N}$ -doped graphene enhancing the electrochemical kinetics for high-performance lithium–sulfur batteries," *J. Mater. Chem. A*, 10.1039/D1TA00800E 9(2021)10704-10713. 10.1039/D1TA00800E. View Article Online
DOI: 10.1039/D1QM00678A
- 451
- 452 [10] Y. Zhao *et al.*, "Preparation and characterization of tungsten oxynitride nanowires," *J Mater Chem*, 17(2007)4436-4440. <https://doi.org/10.1039/B709486H>.
- 453
- 454
- 455 [11] J. Taylor *et al.*, "Theory of rectification in four wires: The role of electrode coupling," *Phys Rev Lett*, 89(2002)138301. <https://doi.org/10.1103/PhysRevLett.89.138301>.
- 456
- 457
- 458 [12] J. P. Perdew *et al.*, "Generalized gradient approximation made simple," *Phys Rev Lett*, 77(1996)3865. 10.1103/PhysRevLett.77.3865.
- 459
- 460
- 461 [13] Y. Zhu *et al.*, "Catalytic activity origin and design principles of graphitic carbon nitride electrocatalysts for hydrogen evolution," *Front. Mater. Sci.*, 6(2019)16. <https://doi.org/10.3389/fmats.2019.00016>.
- 462
- 463
- 464
- 465 [14] A. Ghatak *et al.*, "Pulsed laser assisted growth of aligned nanowires of WO_3 : role of interface with substrate," *RSC Advances*, 10.1039/C5RA27542C 6(2016)31705-31716. 10.1039/C5RA27542C.
- 466
- 467
- 468
- 469 [15] Y. Chen *et al.*, "Thin WS_2 nanotubes from W18O49 nanowires," *Mater. Res. Lett.*, 5(2017)508-515. 10.1080/21663831.2017.1337050.
- 470
- 471
- 472 [16] O. Ola *et al.*, "DFT and experimental studies of iron oxide-based nanocomposites for efficient electrocatalysis," *J. Mater. Chem. C*, 9(2021)6409-6417.
- 473
- 474
- 475 [17] Z. Ma *et al.*, "Effects of WO_x modification on the activity, adsorption and redox properties of CeO_2 catalyst for NO_x reduction with ammonia," *J. Environ. Sci.*, 24(2012)1305-1316.
- 476
- 477
- 478 [18] A. Shpak *et al.*, "XPS studies of the surface of nanocrystalline tungsten disulfide," *J Electron Spectrosc. Relat. Phenom.*, 181(2010)234-238.
- 479
- 480
- 481 [19] F. Perrozzi *et al.*, "Thermal stability of WS_2 flakes and gas sensing properties of WS_2/WO_3 composite to H_2 , NH_3 and NO_2 ," *Sensors and Actuators B: Chemical*, 243(2017)812-822.
- 482
- 483
- 484 [20] V. K. Singh *et al.*, "In situ functionalized fluorescent WS_2 -QDs as sensitive and selective probe for Fe^{3+} and a detailed study of its fluorescence quenching," *ACS Applied Nano Materials*, 2(2018)566-576.
- 485
- 486
- 487
- 488 [21] C. M. Smyth *et al.*, " WSe_2 -contact metal interface chemistry and band alignment under high vacuum and ultra high vacuum deposition conditions," *2D Materials*, 4(2017)025084.
- 489
- 490

- 491 [22] J.-W. Shi *et al.*, "Stable 1T-phase MoS₂ as an effective electron mediator promoting
492 photocatalytic hydrogen production," *Nanoscale*, 10(2018)9292-9303. View Article Online
DOI: 10.1039/D1QM00678A
- 493
- 494 [23] Z. Wang *et al.*, "Roles of N-vacancies over porous g-C₃N₄ microtubes during photocatalytic
495 NO_x removal," *ACS applied materials & interfaces*, 11(2019)10651-10662.
- 496
- 497 [24] F. Wei *et al.*, "Oxygen self-doped gC₃N₄ with tunable electronic band structure for
498 unprecedentedly enhanced photocatalytic performance," *Nanoscale*, 10(2018)4515-4522.
- 499
- 500 [25] A. Ambrosi *et al.*, "2H→ 1T phase transition and hydrogen evolution activity of MoS₂, MoSe
501 ₂, WS₂ and WSe₂ strongly depends on the MX₂ composition," *Chem Commun*, 51(2015)8450-
502 8453.
- 503
- 504 [26] S. Hussain *et al.*, "One-Pot Synthesis of W₂C/WS₂ Hybrid Nanostructures for Improved
505 Hydrogen Evolution Reactions and Supercapacitors," *Nanomaterials*, 10(2020)1597.
- 506
- 507 [27] L. Li *et al.*, "Hierarchical WS(2)@NiCo(2)O(4) Core-shell Heterostructure Arrays Supported on
508 Carbon Cloth as High-Performance Electrodes for Symmetric Flexible Supercapacitors," (in
509 eng), *ACS omega*, 5(2020)4657-4667. 10.1021/acsomega.9b04434.
- 510
- 511 [28] Y. Li *et al.*, "Multifunctional porous nanohybrid based on graphene-like tungsten disulfide on
512 poly(3,4-ethoxylenedioxythiophene) for supercapacitor and electrochemical nanosensing of
513 quercetin," *J. Electrochem. Soc.*, 167(2020)047512. 10.1149/1945-7111/ab721e.
- 514
- 515 [29] W. Yin *et al.*, "Synthesis of tungsten disulfide quantum dots for high-performance
516 supercapacitor electrodes," *J. Alloys. Compd.*, 786(2019)764-769.
517 <https://doi.org/10.1016/j.jallcom.2019.02.030>.
- 518
- 519 [30] X. Qiu *et al.*, "Immobilization of tungsten disulfide nanosheets on active carbon fibers as
520 electrode materials for high performance quasi-solid-state asymmetric supercapacitors," *J.*
521 *Mater. Chem. A*, 10.1039/C8TA01047A 6(2018)7835-7841. 10.1039/C8TA01047A.
- 522
- 523 [31] F. Zheng *et al.*, "Novel diverse-structured h-WO₃ nanoflake arrays as electrode materials for
524 high performance supercapacitors," *Electrochim. Acta*, 334(2020)135641.
525 <https://doi.org/10.1016/j.electacta.2020.135641>.
- 526
- 527 [32] D. M. El-Gendy *et al.*, "Synthesis and characterization of WC@GNFs as an efficient
528 supercapacitor electrode material in acidic medium," *Ceram. Int.*, 46(2020)27437-27445.
529 <https://doi.org/10.1016/j.ceramint.2020.07.230>.
- 530
- 531 [33] X. Zou and Y. Zhang, "Noble metal-free hydrogen evolution catalysts for water splitting,"
532 *Chem. Soc. Rev.*, 10.1039/C4CS00448E 44(2015)5148-5180. 10.1039/C4CS00448E.
- 533

- 534 [34] Z. Huang *et al.*, "Polyoxometallates@zeolitic-imidazolate-framework derived bimetallic tungsten-cobalt sulfide/porous carbon nanocomposites as efficient bifunctional electrocatalysts for hydrogen and oxygen evolution," *Electro. Acta*, 330(2020)135335. <https://doi.org/10.1016/j.electacta.2019.135335>. View Article Online
DOI: 10.1039/D1QM00678A
- 535
- 536
- 537
- 538
- 539 [35] T. P. Nguyen *et al.*, "Facile synthesis of WS₂ hollow spheres and their hydrogen evolution reaction performance," *Appl. Surf. Sci.*, 505(2020)144574. <https://doi.org/10.1016/j.apsusc.2019.144574>.
- 540
- 541
- 542
- 543 [36] J. Wu *et al.*, "Single-atom tungsten-doped CoP nanoarrays as a high-efficiency pH-universal catalyst for hydrogen evolution reaction," *ACS Sustainable Chemistry & Engineering*, 8(2020)14825-14832. 10.1021/acssuschemeng.0c04322.
- 544
- 545
- 546
- 547 [37] H. Tian *et al.*, "Oxygen vacancy-assisted hydrogen evolution reaction of the Pt/WO₃ electrocatalyst," *Journal of Materials Chemistry A*, 10.1039/C8TA12219A 7(2019)6285-6293. 10.1039/C8TA12219A.
- 548
- 549
- 550
- 551 [38] P. V. Sarma *et al.*, "Nanostructured Tungsten Oxysulfide as an Efficient Electrocatalyst for Hydrogen Evolution Reaction," *ACS Catalysis*, 10(2020)6753-6762. 10.1021/acscatal.9b04177.
- 552
- 553
- 554
- 555
- 556
- 557
- 558
- 559
- 560
- 561
- 562
- 563
- 564
- 565
- 566
- 567
- 568
- 569
- 570